Optical nanostructures design, fabrication, and applications for solar/thermal energy conversion

Mool C. Gupta,[1] Craig Ungaro,[1] Jonathan J. Foley IV,[2,3] and Stephen K. Gray[2]

[1]*Department of Electrical & Computer Engineering, University of Virginia, Charlottesville, Virginia, 22901, USA*
[2]*Center for Nanoscale Materials, Argonne National Laboratory, 9700 South Cass Avenue, Argonne, IL, 60439, USA*
[3]*Department of Chemistry, William Paterson University, 300 Pompton Road, Wayne, NJ, 07470, USA*
[1]*mgupta@virginia.edu*
[2]*gray@anl.gov*

Abstract: Optical nanostructures can control the optical absorption and emission properties of surfaces and are therefore being investigated for solar thermophotovoltaics, thermophotovoltaics, solar thermal, infrared sensing, infrared sources, incandescent light sources, and thermal imaging applications, among many others. This review article describes various modeling methods available for design of optical nanostructures to control light absorption and emission properties of surfaces, as well as various methods available for the fabrication of large area nanostructured surfaces. Throughout the review, we provide examples of state of the art energy generation devices using such optical nanostructures. A discussion of outstanding obstacles for the achievement of high efficiency solar thermophotovoltaics systems is provided along with examples of systems showing exceptional promise.

OCIS codes: (220.022) Optical design and fabrication; (230.023) Optical devices; (240.024) Optics at surfaces; (240.031) Thin films; (350.605) Solar Energy; (310.662) Subwavelength structures, nanostructures.

References and links

1. M. Thirugnanasambandam, S. Iniyan, and R. Goic, "A review of solar thermal technologies," Renewable and Sustainable Energy Reviews **14**, 312–322 (2010).
2. Y. Tian and C. Y. Zhao, "A review of solar collectors and thermal energy storage in solar thermal applications," Applied Energy **104**, 538–553 (2013).
3. T. Bauer, *Thermophotovoltaics: basic principles and critical aspects of system design* (Springer, 2011).
4. P. Bermel, M. Ghebrebrhan, W. Chan, Y. X. Yeng, M. Araghchini, R. Hamam, C. H. Marton, K. F. Jensen, M. Soljacic, J. D. Joannopoulos, S. G. Johnson, and I. Celanovic, "Design and global optimization of high-efficiency thermophotovoltaic systems," Opt. Express **18**, A314–334 (2010).
5. N. Harder and P. Wurfel, "Theoretical limits of thermophotovoltaic solar energy conversion," Semiconductor Science and Technology **18**, S151 (2003).
6. C. Ferrari, F. Melino, M. Pinelli, P. R. Spina, and M. Venturini, "Overview and status of thermophotovoltaic systems," Energy Procedia **45**, 1160–1169 (2014).
7. P. Bermel, J. Lee, J. D. Joannopoulos, I. Celanovic, and M. Soljacie, *Selective Solar Absorbers* (Begell House Inc., 2012), chap. 7, Annual Review of Heat Transfer.

8. T. Inoue, M. Zoysa, T. Asano, and S. Noda, "Realization of narrowband thermal emission with optical nanostructures," Optica **2**, 27 (2015).
9. A. Lenert, D. M. Bierman, Y. Nam, W. R. Chan, I. Celanovic, M. Soljacic, and E. N. Wang, "A nanophotonic solar thermophotovoltaic device," Nat. Nanotechnol. **9**, 126–130 (2014).
10. E. Rephaeli and S. Fan, "Absorber and emitter for solar thermophotovoltaic systems to achieve efficiency exceeding the schockley-queisser limit," Opt. Express **17**, 15145–15159 (2009).
11. C. G. Granqvist, "Spectrally selective coatings for energy efficiency and solar applications," Phys. Scripta **32**, 401 (1985).
12. S. Collin, "Nanostructure arrays in free space: optical properties and applications," Rep. Prog. Phys. **77**, 126402 (2014).
13. V. Rinnerbauer, A. Lenert, D. M. Bierman, Y. X. Yeng, W. R. Chan, R. D. Geil, J. J. Senkevich J. D. Joannopoulos, E. N. Wang, M. Soljacic, and I. Cleanovic, "Metallic photonic crystal absorber-emitter for efficient spectral control in high-temperature solar thermophotovoltaics," Advanced Energy Materials **4**, 1400334 (2014).
14. Y. Nam, Y. X. Yeng, A. Lenert, P. Bermel, I. Celanovic, M. Soljačić, and E. N. Wang, "Solar thermophotovoltaic energy conversion systems with two-dimensional tantalum photonic crystal absorbers and emitters," Sol. Energy Mat. Sol. Cells **122**, 287 – 296 (2014).
15. V. Stelmakh, V. Rinnerbauer, W. R. Chan, J. J. Senkevich, J. D. Joannopoulos, M. Soljacic, and I. Celanovic, "Tantalum-tungsten alloy photonic crystals for high-temperature energy conversion systems," Proceedings of the SPIE - The International Society for Optical Engineering **9127**, 91270Q (2014).
16. I. Celanovic, N. Jovanovic, and J. Kassakian, "Two-dimensional tungsten photonic crystals as selective thermal emitters," Appl. Phys. Lett. **92**, 193101 (2008).
17. H. Wang, V. P. Sivan, A. Mitchell, G. Rosengarten, P. Phelan, and L. Wan, "Highly efficient selective metamaterial absorber for high-temperature solar thermal energy harvesting," Sol. Energy Mat. Sol. Cells **137**, 235–242 (2015).
18. X. Liu, T. Tyler, T. Starr, A. Starr, N. Jokerst, and W. Padilla, "Taming the blackbody with infrared metamaterials as selective thermal emitters," Phys. Rev. Lett. **107**, 045901 (2011).
19. I. Khodasevvch, L. Wang, A. Mitchell, and G. Rosengarten, "Micro and nanostructured surfaces for selective solar absorption," Adv. Opt. Mater. **107**, 045901 (2015). doi: 10.1002/adom.201500063.
20. Y. Son, J. Yeo, C. Woo, H. Sukjoon, H. Seung, H. Ko, and D. Yang, "Fabrication of submicron-sized metal patterns on a flexible polymer substrate by femtosecond laser sintering of metal nanoparticles," International Journal of Nanomanufacturing **9**, 468–476 (2013).
21. E. P. B. Filho, O. S. H. Mendoza, C. L. L. Beicker, A. Menezes, and D. Wen, "Experimental investigation of a silver nanoparticle-based direct absorption solar thermal system," Energy Conversion and Management **84**, 261–267 (2014).
22. G. Katumba, L. Olumekor, A. Forbes, G. Makiwa, B. Mwakikunga, J. Lu, and E. Wackelgard, "Optical, thermal and structural characteristics of carbon nanoparticles embedded in ZnO and NiO as selective solar absorbers," Sol. Energy Mater. and Solar Cells **92**, 1285–1292 (2008).
23. A. A. Shah and M. C. Gupta, "Spectral selective surfaces for concentrated solar power receivers by laser sintering of tungsten micro and nano particles," Sol. Energy Mat. Sol. Cells **117**, 489–493 (2013).
24. J. H. Schon, G. Binder, and E. Bucher, "Performance and stability of some new high-temperature selective absorber systems based on metal/dielectric multilayers," Sol. Energy Mat. Sol. Cells **33**, 403–416 (1994).
25. V. K. Narasimhan and Y. Cui, "Nanostructures for photon management in solar cells," Nanophotonics **2**, 187210 (2013).
26. M. C. Gupta, B. K. Nayak, V. Iyengar, and L.Wang, "Efficient light trapping by laser microtexturing of surfaces for photovoltaics," SPIE Newsroom (2012). DOI: 10.1117/2.1201208.004361.
27. M. C. Gupta and D. E. Carlson, "Laser processing for renewable energy materials," MRS Energy and Sustainability: A Review Journal (2015). DOI:10.1557/mre.2015.3.
28. V. V. Iyengar, B. K. Nayak, and M. C. Gupta, "Ultralow reflectance metal surfaces by ultrafast laser texturing," Appl. Opt. **49**, 5983–5988 (2010).
29. A. Luque, "Solar thermophotovoltaics: Combining solar thermal and photovoltaics," AIP Conf. Proc. **890**, 3–16 (2007).
30. V. S. Reddy, S. C. Kaushik, K. R. Ranjan, and S. K. Tyagi, "State-of-the-art of solar thermal power plants-a review," Renew. Sust. Energ. Rev. **27**, 258–273 (2013).
31. R. K. McGovern and W. J. Smith, "Optimal concentration and temperatures of solar thermal power plants," Energ. Convers. Manage. **60**, 226–232 (2012).
32. A. Datas and C. Algora, "Global optimization of solar thermophotovoltaic systems," Progress in Photovoltaics: Research and Applications **21**, 1040–1055 (2013).
33. Y. Xuan, X. Chen, and Y. Han, "Design and analysis of thermophotovoltaic systems," Renew. Energ. **36**, 374–387 (2011).
34. K. A. Arpin, M. D. Losego, and P. V. Braun, "Electrodeposited 3D tungsten photonic crystals with enhanced thermal stability," Chemistry of Materials **23**, 4783–4788 (2011).
35. C. Ungaro, S. K. Gray, and M. C. Gupta, "Black tungsten for solar power generation," Appl. Phys. Lett. **103**, 071105–071105–3 (2013).

36. H. Sai and H. Yugami, "Thermophotovoltaic generation with selective radiators based on tungsten surface gratings," Appl. Phys. Lett. **85**, 3399–3401 (2004).
37. H. Sai, Y. Kanamori, K. Hane, H. Yugami, and M. Yamaguchi, "Numerical study on tungsten selective radiators with various micro/nano structures," Photovoltaic Specialists Conference pp. 762–765 (2005).
38. Y. B. Chen and Z. M. Zhang, "Design of tungsten complex gratings for thermophotovoltaic radiators," Opt. Comm. **269**, 411–417 (2007).
39. E. B. Grann and M. G. Moharam, "Comparison between continuous and discrete subwavelength grating structures for antireflection surfaces," J. Opt. Soc. Am. **13**, 988–922 (1996).
40. C. Ungaro, S. K. Gray, and M. C. Gupta, "Graded-index structures for high-efficiency solar thermophotovoltaic emitting surfaces," Opt. Lett. **39**, 5259–5262 (2014).
41. S. K. Gray, "Theory and modeling of plasmonic structures," J. Phys. Chem. C **117**, 1983–1994 (2013).
42. A. Taflove and S. C. Hagness, *Computational Electrodynamics: the Finite-Difference Time-Domain Method* (Artech, 2000).
43. A. F. Oskooi, D. Roundy, M. Ibanescu, P. Bermel, J. D. Joannopoulos, and S. G. Johnson, "Meep: A flexible free-software package for electromagnetic simulations by the FDTD method," Comp. Phys. Comm. **181**, 687702 (2010).
44. C. F. Bohren and D. R. Huffman, *Absorption and Scattering of Light by Small Particles* (John Wiley and Sons, 1998).
45. P. Yeh, *Optical Waves in Layered Media* (Wiley, 2005).
46. B. T. Draine and P. J. Flatau, "Discrete-dipole approximation for scattering calculations," J. Opt. Soc. Am. A **11**, 1491–1499 (1994).
47. J. M. McMahon, "Topics in theoretical and computational nanoscience: From controlling light at the nanoscale to calculating quantum effects with classical electrodynamics," Ph.D. thesis, Northwestern University (2011).
48. M. G. Moharam, D. A. Pommet, E. B. Grann, and T. K. Gaylor, "Stable implementation of the rigorous coupled-wave analysis for surface-relief gratings: enhanced transmittance matrix approach," J. Opt. Soc. A **12**, 1077 (1995).
49. L.-L. Lin, Z.-Y. Li, and K.-M. Ho, "Lattice symmetry applied in transfer-matrix methods for photonic crystals," J. Appl. Phys. **98**, 811 (2003).
50. H. Saia, H. Yugamia, Y. Kanamorib, and K. Hane, "Solar selective absorbers based on two-dimensional W surface gratings with submicron periods for high-temperature photothermal conversion," Sol. Energy Mat. Sol. Cells **79**, 35–49 (2003).
51. V. Rinnerbauer, Y. Shen, J. D. Joannopolous, M. Soljačić, F. Schäffler, and I. Celanovic, "Superlattice photonic crystal as broadband solar absorber for high temperature operation," Opt. Express **22**, A1895 (2014).
52. R. G. Barrerra, M. del Castillo-Mussot, G. Monsivais, P. Villaseor, and W. L. Mochán, "Optical properties of two-dimensional disordered systems on a substrate," Phys. Rev. B **38**, 5371 (1988).
53. R. G. Barrerra, G. Monsivais, and W. L. Mochán, "Renormalized polarizability in the maxwel garnett theory," Phys. Rev. B **43**, 13819 (1991).
54. S. Yoo and Q.-H. Park, "Effective permittivity for resonant plasmonic nanoparticle systems via dressed polarizability," Opt. Express **20**, 16480 (2012).
55. H. A. Atwater and A. Polman, "Plasmonics for improved photovoltaic devices," Nature Mater. **9**, 205–213 (2010).
56. J. M. Geffrin, B. García-Cámara, R. Góomez-Medina, P. Albella, L. S. Froufe-Pérez, C. Eyraud, A. Litman, R. Vaillon, F. González, M. Nieto-Vesperinas, J. J. Sáenz, and F. Moreno, "Magnetic and electric coherence in forward- and back-scattered electromagnetic waves by a single dielectric subwavelength sphere," Nat. Commun. **3**, 1171 (2012).
57. J. R. Cole and N. J. Halas, "Optimized plasmonic nanoparticle distributions for solar spectrum harvesting," Appl. Phys. Lett. **89**, 153120 (2006).
58. K. T. Fountaine, C. G. Kendall, and H. A. Atwater, "Near-unity broadband absorption designs for semiconducting nanowire arrays via localized radial mode excitation," Opt. Express **22**, A930 (2014).
59. P. Spinelli, M. A. Verschuuren, and A. Polman, "Broadband omnidirectional antireflection coating based on subwavelength surface Mie resonators," Nat. Commun. **3**, 692 (2012).
60. E. Rephaeli and S. Fan, "Tungsten black absorber for solar light with wide angular operation range," Appl. Phys. Lett. **92**, 211107 (2008).
61. P. Ben-Adballah and B. Ni, "Single-defect bragg stacks for high-power narrow-band thermal emission," J. Appl. Phys **97**, 104910 (2005).
62. B. J. Lee and Z. M. Zhang, "Design and fabrication of planar multilayer structures with coherent thermal emission characteristics," J. Appl. Phys **100**, 063529 (2006).
63. J. J. Foley IV, C. Ungaro, K. Sun, M. C. Gupta, and S. K. Gray, "Design of emitter structures based on resonant perfect absorption for thermophotovoltaic applications," Opt. Express **23**, A1373 (2015).
64. J. J. Foley IV, J. M. McMahon, G. C. Schatz., H. Harutyunyan, G. P. Wiederrecht, and S. K. Gray, "Inhomogeneous surface plasmon polaritons," ACS Photonics **1**, 739–745 (2014).
65. P. C. Chang, J. G. Walker, and K. I. Hopcraft, "Ray tracing in absorbing media," J. Quant. Spectrosc. Radiat. Transfer **96**, 327–341 (2005).

66. L. Wendler and R. Haupt, "An improved virtual mode theory of ATR experiments of surface polaritons," Phys. Stat. Sol. b **143**, 131–147 (1987).
67. S. M. Maier, *Plasmonics: Fundamentals and Applications* (Springer, 2007).
68. L. Novotny and B. Hecht, *Principles of Nano-Optics* (Cambridge University, 2012), 2nd ed.
69. J. J. Foley IV, H. Harutyunyan, D. Rosenmann, R. Divan, G. P. Wiederrecht, and S. K. Gray, "When are surface plasmon polaritons excited in the Kretschmann-Raether configuration?" Sci. Rep. **5**, 09929 (2015).
70. E. F. C. Driessen and M. J. A. de Dood, "The perfect absorber," Appl. Phys. Lett. **94**, 171109 (2009).
71. M. A. Kats, D. Sharma, J. Lin, P. Genevet, R. Blanchard, Z. Yang, M. M. Qazilbash, D. N. Basov, S. Ramanathan, and F. Capasso, "Ultra-thin perfect absorber employing a tunable phase change material," App. Phys. Lett. **101**, 221101 (2012).
72. M. A. Kats, R. Blachard, P. Genevet, and F. Capasso, "Nanometer optical coatings based on strong interference effects in highly absorbing media," Nat. Mat. **12**, 20–24 (2013).
73. H. Raether, *Surface Plasmons on Smooth and Rough Surfaces and on Gratings* (Springer-Verlag, 1988).
74. J. Drevillon and P. Ben-Abdallah, "*Ab initio* design of coherent thermal sources," J. Appl. Phys. **102**, 114305 (2007).
75. E. Nefzaoui, J. Drevillon, and K. Joulain, "Selective emitters design and optimization for thermophotovoltaic applications," J. Appl. Phys. **111**, 084316 (2012).
76. M. Shimizu, A. Kohiyama, and H. Y. Yugami, "High-efficiency solar-thermophotovoltaic system equipped with a monolithic planar selective absorber/emitter," J. Photon. Energy **5**, 053099–53107 (2015).
77. A. W. Rodriguez, O. Ilic, P. Bermel, I. Celanovic, J. D. Joannopoulos, M. Soljacic, and S. G. Johnson, "Frequency-selective near-field radiative heat transfer between photonic crystal slabs: A computational approach for arbitrary geometries and materials," Phys. Rev. Lett. **107**, 114302 (2011).
78. A. Datas, D. Hirashima, and K. Hanamura, "FDTD simulation of near-field radiative heat tansfer between thin films supporting surface phonon polaritons: Lessons learned," J. Therm. Sci. Tech. **8**, 91–105 (2013).
79. A. Didari and M. P. Menguc, "Analysis of near-field radiation transfer within nano-gaps using FDTD method," J. Quant. Spect. Radiat. Transf. **146**, 214–226 (2014).
80. A. Didari and M. P. Menguc, "Near-field thermal emission between corrugated surfaces separated by nano-gaps," J. Quant. Spect. Radiat. Transf. **158**, 43–51 (2015).
81. K. Aydin, V. E. Ferry, R. M. Briggs, and H. A. Atwater, "Broadband polarization-independent resonant light absorption using ultrathin plasmonic super absorbers," Nature Comm. **2**, 517 (2011).
82. Lumerical Solutions, Inc., http://www.lumerical.com/tcad-products/mode/.
83. M. A. Yurkin, M. Min, and A. G. Hoekstra, "Applicaton of the discrete dipole approximation to very large refractive indices: Filtered doupled dipoles revived," Phys. Rev. E **82**, 036703 (2010).
84. V. L. Y. Loke and M. P. Menguc, "Surface waves and atomic force microscope probe-particle near-field coupling: discrete dipole approximation with surface interaction," J. Opt. Soc. Am. A **27**, 2293–2303 (2010).
85. S. Edalatpour and M. Francoeur, "The thermal discrete dipole approximation (t-dda) for near-field radiative heat transfer simulations in three-dimensional arbitrary geometries," J. Quant. Spect. Radiat. Transf. **133**, 364–373 (2015).
86. J. A. Nelder and R. Mead, "A simplex method for function minimization," Comp. J. **7**, 308–313 (1965).
87. A. Lin and J. Phillips, "Optimization of random diffraction gratings in thin-film solar cells using genetic algorithms," Sol. Energy Mat. Sol. Cells **92**, 1689–1696 (2008).
88. M. Clerc, *Particle Swarm Optimization* (Wiley, 2008).
89. R. L. Miller, Z. Xie, S. Leyffer, M. J. Davis, and S. K. Gray, "Surrogate-based modeling of the optical response of metallic nanostructures," J. Phys. Chem. C **114**, 20741–20748 (2010).
90. V. V. Iyengar, B. K. Nayak, and M. C. Gupta, "Optical characteristics of femtosecond laser micromachined periodic structures in Si 100," Appl. Opt. **45**, 7137–7143 (2006).
91. M. C. Gupta and S. T. Peng, "Diffraction characteristics of surface-relief gratings," Appl. Opt. **32**, 2911–2917 (1993).
92. W. M. Steen and J. Mazumder, *Laser Material Processing* (Springer, 2010), 4th ed.
93. M. M. Hawkeye, M. T. Tashuk, and M. J. Brett, *Glancing Angle Deposition of Thin Films: Engineering the Nanoscale* (Wiley, 2014).
94. C. Ungaro, A. Shah, I. Kravchenko, D. K. Hensley, S. K. Gray, and M. C. Gupta, "Optical and infrared properties of glancing angle deposited nanostructured tungsten films," Opt. Lett. **40**, 506–509 (2015).
95. N. Selvakumar and H. Barshilia, "Review of physical vapor deposited (pvd) spectrally selective coatings for mid- and high-temperature solar thermal applications," Sol. Energy Mat. Sol. Cells **98**, 1–23 (2012).
96. C. E. Kennedy, "Review of mid-to-high temperature solar selective absorber materials. technical report nrel/tp-520-31267," Tech. rep., National Renew. Energ. Laboratory (2002).
97. X. Li, Y. Chen, J. Miao, P. Zhou, Y. Zheng, and L. Chen, "High solar absorption of a multilayered thin film structure," Opt. Express **15**, 1907–1912 (2007).
98. N. P. Sergeant, O. Pincon, M. Agrawal, and P. Peumans, "Design of wide-angle solar-selective absorbers using aperiodic metal-dielectric stacks," Opt. Express **17**, 22800–22812 (2009).
99. N. P. Sergeant, M. Agrawal, and P. Peumans, "High performance solar-selective absorbers using coated sub-

wavelength gratings," Opt. Express **18**, 5525–5540 (2010).
100. S. Esposito, A. Antonaia, M. Addonizio, and S. Aprea, "Fabrication and optimization of highly efficient cermet-based spectrally selective coatings for high operating temperature," Thin Solid Films **517**, 6000–6006 (2009).
101. L. T. A. Berghaus, A. Djahanbakhsh, "Characterisation of cvd - tungsten alumina cermets for high-temperature selective absorbers," Sol. Energy Mat. Sol. Cells **54**, 19–26 (1998).
102. M. Farooq and M. Hutchins, "Optical properties of higher and lower refractive index composites in solar selective coatings," Sol. Energy Mat. Sol. Cells **71**, 73–83 (2002).
103. D. Xinkang, W. Cong, W. Tianmin, Z. Long, C. Buliang, and R. Ning, "Microstructure and spectral selectivity of Mo-Al_2O_3 solar selective absorbing coatings after annealing," Thin Solid Films **516**, 3971–3977 (2008).
104. Q. Zhang, Y. Yin, and D. Mills, "High efficiency Mo-Al_2O_3 cermet selective surfaces for high-temperature applications," Sol. Energy Mat. Sol. Cells **40**, 43–53 (1996).
105. Q. Zhang, "Recent progress in high-temperature solar selective coatings," Sol. Energy Mat. Sol. Cells **62**, 63–74 (2000).
106. R. Schmidt and K. Park, "High-temperature space-stable selective solar absorber coatings," Appl. Opt. **4**, 917–925 (1965).
107. C. Schlemmer, J. Aschaber, V. Boerner, and J. Luther, "Thermal stability of micro-structured selective tungsten emitters," Thermophotovoltaic Generation of Electricity: 5th Conference, CP653 - American Institute of Physics (2003).
108. V. Rinnerbauer, S. Ndao, Y. X. Yeng, W. R. Chan, J. J. Senkevich, J. D. Joannopoulos, M. Soljacic, and I. Celanovic, "Recent developments in high-temperature photonic crystals for energy conversion," Energy and Environmental Science (2012).
109. F. Ghmari, T. Ghbara, M. Laroche, R. Carminati, and J.-J. Greffet, "Influence of microroughness on emissivity," Journal of Applied Physics **96**, 2656–2664 (2004).
110. A. Lasagni, M. Nejati, R. Clasen, and F. Mucklich, "Periodical surface structuring of metals by laser interference metallurgy as a new fabrication method of textured solar selective absorbers," Adv. Eng. Mater. **8**, 580–584 (2006).
111. M. Saidi and R. H. Abardeh, "Air pressure dependence of natural-convection heat transfer," Proceedings of the World Congress on Engineering 2010 **II** (2010).
112. W. Shockley and H. J. Queisser, "Detailed balance limit of efficiency of p-n junction solar cells," J. Appl. Phys **32**, 510–519 (1961).
113. J. Wang, B. Wei, Q. Wei, and D. Li, "Optical property and thermal stability of Mo/Mo-SiO_2/SiO_2 solar-selective coating prepared by magnetron sputtering," Physica Status Solidi A **208**, 664–667 (2011).
114. A. Lenert, D. M. Bierman, Y. Nam, W. R. Chan, I. Celanovic, M. Soljacic, and E. N. Wang, "A nanophotonic solar thermophotovoltaic device," Nat. Nanotechnol. **9**, 126–130 (2014).
115. A. S. Vlasov, V. P. Khvostikov, O. A. Khvostikova, P. Y. Gazaryan, S. V. Sorokina, and V. M. Andreev, "TPV systems with solar powered tungsten emitters," AIP Conference Proceedings **890**, 327–334 (2007).
116. E. D. Palik, *Handbook of Optical Constants of Solids* (Academic, 1998).
117. H. Yugami, H. Sai, K. Nakamura, H. Nakagawa, and H. Ohtsubo, "Solar thermophotovoltaic using Al_2O_3/$Er_3Al_5O_{12}$ eutectic composite selective emitter," IEEE Photovoltaic Specialists Conference **28**, 1214–1217 (2000).
118. A. Datas and C. Algora, "Development and experimental evaluation of a complete solar thermophotovoltaic system," Progress in Photovoltaics: Research and Applications **890**, 327–334 (2012).
119. C. Ungaro, "Control of optical properties of surfaces for improved solar thermophotovoltaic systems," Phd thesis, University of Virginia (2015).
120. S. Lin, J. Moreno, and J. G. Fleming, "Three-dimensional photonic-crystal emitter for thermal photovoltaic power generation," Appl. Phys. Lett. **83**, 380–382 (2003).
121. C. Wu, B. N. III, J. John, A. Milder, B. Zollars, S. Savoy, and G. Shvets, "Metamaterial-based integrated plasmonic absorber/emitter for solar thermo-photovoltaic systems," J. Optics **14**, 24005–24008 (2012).
122. C. Ungaro, S. K. Gray, and M. C. Gupta, "A solar thermophotovoltaic system using nanostructures," Opt. Express **23**, A111–A1119 (2015).

1. Introduction

Recently, there has been strong research activity in solar thermal (ST) [1, 2], solar thermophotovoltaic (STPV) [3–5], and thermophotovoltaic (TPV) [6, 7] energy conversion. To provide a state of the art status in these fields, we have prepared this review article. There is strong potential for growth in these areas, especially through the use of novel nanostructured surfaces to control light absorption and emission from surfaces and to achieve high efficiency. This spectral light control can be achieved by nanostructuring of surfaces, which can strongly modify their optical properties [8–10]. Recently, significant progress has been made in the modeling

and fabrication of nanostructures to control optical absorption and emission properties of surfaces. Nanostructured surfaces, for example, can be designed to be significantly more absorbing than their flat counterparts. Similarly, surfaces can be designed to emit infrared radiation in a very narrow spectral range, providing spectrally selective surfaces [11, 12]. Figure 1 shows the change in emission spectra from a blackbody emitter to a selective emitter using optical nanostructures. Some typical nanostructures are depicted schematically in Fig. 2.

STPV, ST, and TPV systems all share common surfaces but operate under different conditions. ST and STPV systems offer an alternative to PV power generation in alternative energy systems. Since both are heat engines, they do not adhere to the Shockley-Queisser limit and can theoretically exhibit extremely high efficiencies. Additionally, since both ST and STPV systems rely on elements heated to high temperatures via concentrated solar energy, they are easy to modify for thermal storage of energy. This would allow them to operate into the night. An advantage of ST systems over STPV systems is that ST systems do not require the use of PV cells. The PV cells in STPV systems are expensive and can limit overall system size. Conversely, an advantage of STPV systems over ST systems is that STPV systems have no thermal fluid or moving parts. This leads to them being more stable and compact solutions. Overall, ST tends to lend itself to large, immobile power installations while STPV is better suited for small applications. TPV systems operate on the same principle as STPV systems, but rely on an external heat source instead of solar energy. This allows them to be used in energy reclamation systems.

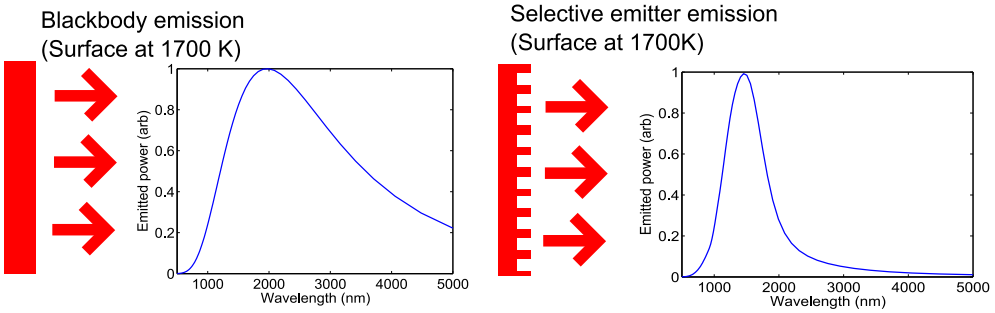

Fig. 1: Spectral emission of a blackbody vs. a selective emitter. Note that the scales on each graph are in different arbitrary units; the graph is intended to show the relative narrowness of the spectrum using the selective emitter.

Fig. 2: Types of nanostructured absorbing and emitting surfaces: a) random nanotexture b) periodic nanotexture and c) dielectric/metal stack.

Such control of light absorption and emission properties allows the design of high efficiency solar and thermal energy conversion devices. It also has applications in the development of high efficiency infrared sources, sensors, and incandescent light sources. Various approaches have been demonstrated for controlling light absorption and emission from surfaces such as the use of photonic crystals [13–16], optical metamaterials [17–19], nanoparticles [20–23], multilayer thin films [10,24] and micro/nano textured structures [25–28]. This review article describes various modeling methods available for design of optical nanostructures to control light absorption

and emission properties of surfaces, the various methods available for the fabrication of large area nanostructured surfaces, and provides some examples of high-efficiency, state of the art, energy generation devices using such optical nanostructures. A path forward to more efficient solar and thermal energy generation devices using practical design methods and fabrication techniques is examined.

The limiting efficiency for ST and STPV systems with ideal absorbing and emitting surfaces comes from the Carnot efficiency (η) given by $\eta = 1 - \frac{T_c}{T_h}$, where T_c and T_h are the hot and cold temperatures, respectively. The absorbing surface efficiency is lowered due to radiative loss, given by $A\varepsilon\sigma T^4$, where A is the area, ε is emissivity, σ is the Stefan-Boltzmann constant, and T is temperature. While the Carnot efficiency of the system will increase with temperature, the absorbing surface efficiency will decrease due to increased emission from the absorbing surface at high operating temperatures [29]. The maximum operating efficiency of 85.4% is therefore reached at an operating temperature of 2600 K in the ideal case for both systems. Increasing the temperature beyond this will result in a decrease in system efficiency. This analysis assumes that incoming radiation is concentrated to the maximum achievable solar concentration of 46000x. At this concentration, the ideal surface is simply a blackbody absorber.

As the solar concentration is decreased, the ideal surface will be a blackbody absorber for wavelengths below some λ_{cutoff}, and an ideal reflector (generating lower emission) for wavelengths above the cutoff. The location of λ_{cutoff} depends on the temperature of the system, the power density of the emission from the emitter, and the solar concentration levels achieved in the system. Typical λ_{cutoff} values will be close to 2 μm due to the importance of absorbing a large portion of the solar spectrum [10].

In the case of STPV systems, the emitting surface will also play a role in device efficiency. The ideal surface will be a monochromatic emitter that emits radiation with energy equal to the bandgap energy of the PV cell used in the system [29]. Unfortunately, monochromatic emitters have a power density of 0, resulting in the requirement of an infinitely large emitting surface for practical power generation. Therefore, in practical STPV systems, an emitting surface with a small bandwidth will be desirable [10]. Figure 3 shows the evolution of maximum system efficiency vs. temperature for an ideal system.

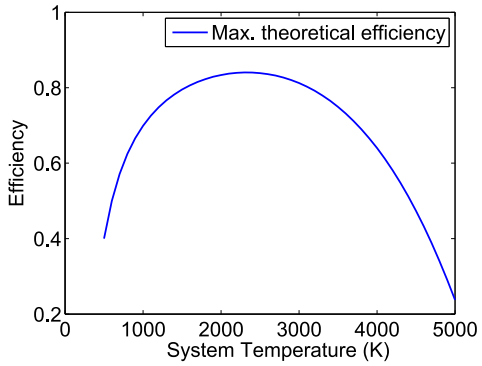

Fig. 3: Maximum theoretical efficiency for various system temperatures. Note the fast increase around typical operation temperatures for ST and STPV systems.

The temperature of 1000°C was an upper limit chosen for practical ST systems based off existing technologies [2,30]. This temperature was chosen for the purpose of comparing different nanostructured surfaces suitable for incorporation into ST systems. The performance of ST

systems will generally increase up to a specific temperature [31]. The value of this temperature is dependent on the quality of surfaces used and the solar concentration value achieved. For tower-based (high-concentration) ST systems, this temperature is usually significantly above current operating temperatures, resulting in a desire for increased thermal stability. Most materials degrade at high temperatures for extended period of operation, so a reasonable number of 1000° was assumed. This number is consistent with temperature used in many solar thermal applications as well as for thermophotovoltaics.

Figure 2 shows different kinds of nanostructures used to create spectrally selective surfaces in energy generation systems. Random and periodic nanostructures may have different shapes depending on the fabrication method used. Triangular, sawtooth, square, spherical, and cylindrical structures all see use in these systems [10, 32, 33]. Additionally, spherical or obloid nanostructures may be embedded in a dielectric matrix to selectively scatter specific wavelengths of light. Lastly, as shown in Figure 2c, planar dielectric or dielectric and metal stacks may be used.

Melting point depression and thermal mismatching between layers makes temperature stability a major concern for spectrally selective surfaces. This issue is solved primarily through material selection and the use of protective coatings on nanostructured materials [34]. Smaller nanostructures and thinner layers can increase this effect, resulting in a limited design space for some nanomaterials.

The type of nanostructure used in a system can have a large impact on its ease of fabrication, spectral selectivity, and temperature stability. The use of random elements in nanostructures eases fabrication tolerance requirements and can improve selectivity, but can be difficult to design for or simulate properly [35]. The presence of some smaller–period nanostructures can lead to lower thermal stability in random nanostructures as well.

Square and cylindrical type gratings result in a rapid change in index of refraction (as compared to tapered structures) that can result in low visible or near infrared (IR) emittance and narrow absorption peaks [36, 37]. This can be a boon to the design of narrow-band emitter structures, or a hindrance to the design of solar absorbing surfaces. Combinations of multiple periods of gratings can be used to broaden the emittance peaks in these structures; however, they still lack high emission in the near IR and visible regions [38]. Using conical, sawtooth, or triangular type nanostructures can increase short-wavelength emission due to the more gradual change in index throughout the structure [39, 40]. Planar surfaces using thin layers of multiple different dielectrics suffer from relatively broad absorption peaks. The inclusion of a metallic layer or the addition of many dielectric layers can result in a much more narrow emission peak [10].

There are many examples in the literature of nanostructures being applied to make high efficiency systems. Wang *et al.* [17] have demonstrated a highly efficient selective metamaterial absorber for high-temperature solar thermal energy harvesting. Using nanostructured titanium gratings on a MgF_2 spacer deposited on W thin films was demonstrated with UV-near IR absorption of 0.9 and mid-IR emittance of 0.2. A structure with solar to heat conversion efficiency of 80% at 400°C was modeled and fabricated to achieve high solar light absorption efficiency over broad spectral wavelength range and emission surfaces emitting in a narrow band of wavelengths.

Spectrally selective surfaces have also been achieved by depositing nanoparticles on a surface and modifying surface morphology. Shah *et al.* [23] investigated spectrally selective surfaces for concentrated solar power receivers by laser sintering of tungsten micro and nanoparticles on a stainless steel substrate, resulting in a solar absorptance of 83% and thermal emittance of 11.6% at room temperature. Multi-layer thin films of metal-dielectric coatings have also been shown to provide high broad wavelength solar absorption and low thermal emittance [24].

The use of theory and modeling has been critical to the design of these types of record-

breaking structures, and will no doubt be critical moving forward as the community continues to push the limits of conversion efficiency, durability, affordability, etc. In the following section, we will try to illustrate how theoretical electrodynamics techniques can be brought to bear to design these types of structures, as well as what challenges exist.

2. Design methodologies

2.1. Overview of the theoretical foundations of the optical properties of nanostructures

Understanding how a nanostructured surface or particle absorbs, scatters, and/or reflects incident light provides critical information enabling the design of systems for efficient solar energy conversion. Calculating these quantities depends upon the ability to solve Maxwell's equations when light is incident upon nanostructures [41]. A wide variety of theoretical methodologies exist for solving Maxwell's equations either in the time-domain (see for example [42, 43]), or in the frequency domain (see for example [44–49]). Time-dependent approaches of solving Maxwell's equations typically start from the first-order time-dependent electric and magnetic field equations, whereas frequency domain methods usually take the second-order frequency-dependent wave equation, supplemented by appropriate boundary conditions, as their starting point.

In a few cases, Maxwell's equations can be solved analytically; indeed, under some often reasonable approximations, the analytical solutions can even be written simply, which greatly aids intuition about the behavior of a nanostructure. Two important analytical examples we will consider include the interaction of light with spherical nanostructures, solvable by Mie theory, and the interaction of light with planar nanostructures, solvable by the Transfer Matrix method. For more general structures, numerical techniques must be employed, and several approaches have been put to considerable use. Here we will discuss the finite-difference time-domain (FDTD) method and the discrete dipole approximation (DDA); the former solves Maxwell's equations in the time-domain, while the latter solves them in the frequency-domain. Two other frequency-domain approaches, that we do not focus in detail on, should also be noted. The finite element method, or FEM, is a frequency-domain approach capable of describing a greater variety of problems than DDA [47]. The vectorial nature of Maxwell's equations make implementations of FEM significantly more sophisticated than DDA. Rigorous coupled-wave analysis (RCWA) represents another frequency-domain method for solving Maxwell's equations that is particularly relevant for periodic structures [48, 49] and, because of its efficiency, has been used successfully to design a number of absorber and emitter structures for TPV/STPV applications, see for example [50, 51]. In what follows we will also give several examples of applications of nanostructures for solar energy conversion, focusing on which of the above methodologies are most appropriate, and how they would be utilized for designing these nanostructures.

2.2. Mie theory for spherical nanostructures

Mie theory provides an analytical solution for Maxwell's equations when light is incident upon a spherical particle. Analytical solutions are available for not only homogeneous spheres but spheres composed of a core sphere with one or more outer shells, and arbitrary complex dielectric constants may be used to define the spherical systems. Quantities like the absorption, scattering, and extinction cross section of the particle can be easily computed with Mie theory. An excellent discussion of Mie theory, as well as practical source code, can be found in [44].

While only rigorous for isolated spherical particles in homogeneous media, judicious use of Mie theory can be an invaluable tool for modeling more complicated structures. For instance, Mie theory can be adapted for very small particles that can be modeled as ellipsoids, which includes nanodisks, nanorods, etc. [44] Similarly, Mie theory can be combined with effective medium theories, e.g. Maxwell-Garnett theory, to model regular or random arrays of particles

on a substrate, provided that the coupling between the neighboring particles is negligible [44]. Extensions to effective medium theories have also been developed that account for the impact on near-neighbor coupling on the polarizability of a spherical structure, including renormalized polarizability approaches of Mochán and co-workers [52, 53], and dressed polarizability approaches of Yoo *et al.* [54]. These approaches offer similar simplicity of using Mie theory in conjunction with an effective medium theory, but offer a more rigorous treatment of the coupled optical response of the spherical particle to its neighbors.

2.3. Design of nanostructures for enhancing solar energy conversion using Mie theory

The relative simplicity of the theoretical framework describing scattering and absorption of spherical nanostructures affords the ability to design systems utilizing spherical nanoparticles for a variety of solar conversion applications. The scattering properties of spherical nanoparticles can be leveraged to concentrate and trap incident light into thin-film photovoltaic (PV) materials to increase their conversion efficiency. This strategy is particularly effective if the light scattering can occur only in the forward direction, increasing the flux of optical energy into an active PV material, for example [55]. Mie theory leads to the prediction of this particularly extreme form of anisotropy where the particles scatter light only in the forward direction when the coefficients for the electric and magnetic dipolar terms (a_1 and b_1, respectively) are identical, which is often called the first Kerker condition [56]. Physically, this can be understood as an interference between electric and magnetic dipolar resonances. Because this is a resonant effect, a given particle geometry will support such scattering behavior only at certain frequencies. Nevertheless, Mie theory computes these coefficients directly, and it is straightforward to develop a design protocol for spherical particles embedded in a medium with known optical properties (e.g. corresponding to the PV material, or a compatible substrate) that support these resonances at a desired frequency. The exceptionally large extinction cross sections of metal nanoparticles, due to their ability to support surface plasmons, can also be exploited to efficiently trap light across the solar spectrum. For example, the optical response of spherical dielectric-core metal-shell nanoparticles is highly tunable, and can be computed exactly with a generalization of Mie theory. Halas and co-workers have employed Mie theory to design optimal distributions of core-shell nanoparticles to enhance absorption over the AM 1.5 solar spectrum [57], where AM 1.5 indicates the standard for the solar spectrum after attenuation by Earth's atmosphere. Using a distribution of simple silica core/gold shell particles with modest coverage allowed absorption of 84% of incident solar power across the AM 1.5 spectrum [57]. Figure 4 shows the extinction efficiency computed by Mie theory for various core-shell particle structures. Similarly, resonant or near-resonant scattering effects of spherical or cylindrical nanostructures, including nanowires, have been modeled within the framework of Mie theory to create exceptionally strong broad-band absorbing structures [58] and broad-band anti-reflection coatings [59], both of which are widely applicable to solar conversion technologies. Again, we emphasize that Mie theory is rigorous only in the limit of isolated particles in homogeneous media and cannot easily account for particle/interface effects. For such effects, more general numerical modeling approaches such as FDTD or DDA are required, and we discuss these approaches in Sections 2.6-2.8.

2.4. Transfer Matrix Methods for planar structures

For multi-layer planar structures, the fields can be written piece-wise as plane waves, and closed-form expressions for the wavevectors and amplitudes of the fields in each layer can be determined from considerations of Maxwell's equations and appropriate boundary conditions. The boundary conditions can be expressed conveniently as matrix equations, and the amplitudes can be computed by straightforward matrix multiplication, which forms the basis of what

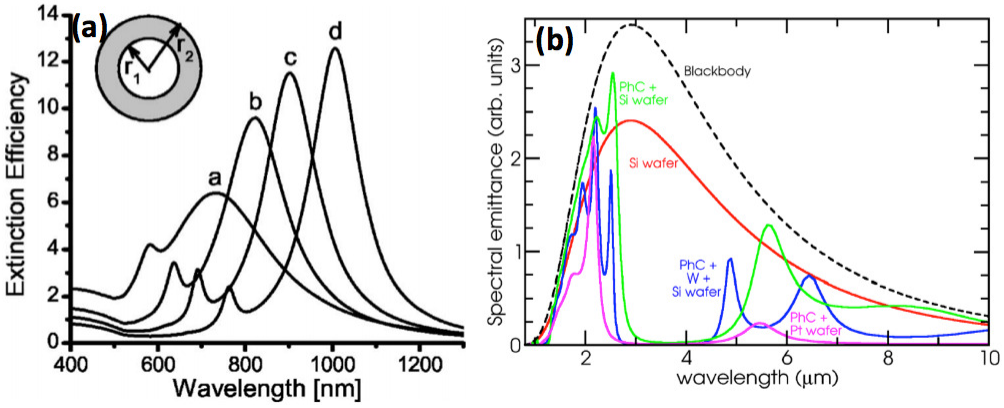

Fig. 4: Illustration of radiation control using engineered spherical core-shell nanoparticles **(a)** and multi-layer planar film structures **(b)**. The absorption, scattering, and extinction cross sections of the core-shell particles can be tuned across the solar spectrum by changing the ratio of the shell thickness (r_2) to the core radius (r_1), and these quantities can be computed using Mie theory (see Section *2.2*) for isolated particles, or the DDA method (see Section *2.8*) for assemblies of particles. In **(a)**, the radius of a silica core is fixed at 60 nm, and the thickness of a gold shell is taken to be 80 nm for curve **a**, 70 nm for curve **b**, 67 nm for curve **c**, and 65 nm for curve **d**. The emittance of several multi-layer structures plotted in **(b)** can be simply computed using the Transfer Matrix Method (see Section *2.4*); however, more sophisticated global device efficiency considerations were used to identify a photonic crystal on a platinum substrate (violet curve in **(b)** as the optimal emitter structure for an integrated STPV system [4]. Figures reproduced from [57] and [4] with permission.

is called the Transfer Matrix Method [45]. The general Transfer Matrix equations for an L-layer system can be written as

$$\begin{pmatrix} E_1^+ \\ E_1^- \end{pmatrix} = \begin{pmatrix} M_{1,1} & M_{1,2} \\ M_{2,1} & M_{2,2} \end{pmatrix} \begin{pmatrix} E_L^+ \\ E_L^- \end{pmatrix}, \tag{1}$$

where the elements $M_{i,j}$ depend on the material properties (the refractive index, n) and geometry of each layer, as well as the frequency and polarization of incident light. The precise form of these elements can be found in the excellent treatment by Yeh [45], and this method has been successfully applied for designing multi-layer absorbing structures that find wide use in TPV/STPV applications [61–63]. We interpret E_1^+ and E_1^- as incoming and outgoing wave amplitudes on the incident side, respectively; similarly, E_L^- and E_L^+ are incoming and outgoing wave amplitudes, respectively, on the terminal side of the structure. With the access to the field amplitudes and wavevectors, a number of useful quantities may be computed. For example, the Fresnel reflection and transmission amplitudes may be computed as $r = E_1^-/E_1^+ = M_{2,1}/M_{1,1}$ and $t = E_L^+/E_1^+ = 1/M_{1,1}$, respectively. The reflection can then be calculated as $R = |r|^2$, the transmission as $T = |t|^2 n_L \cos(\theta_L)/(n_1 \cos(\theta_1))$, where n_i and θ_i denote the refractive index and incident/refraction angle for layer i, with $i = 1$ and L being the semi-infinite layers that surround the structure. This equation is valid provided that the waves incident from layer 1 and transmitted into layer L have real propagation constants (i.e. real refractive indices and associated angles). The intermediate layers 2, ..., L-1 may have complex refractive indices and angles [45]. For computing the Fresnel equations, the field amplitude E_L^- is set to zero and the amplitude E_1^+ is set to 1 by convention. The absorption can simply be computed as $A = 1 - T - R$. Thus,

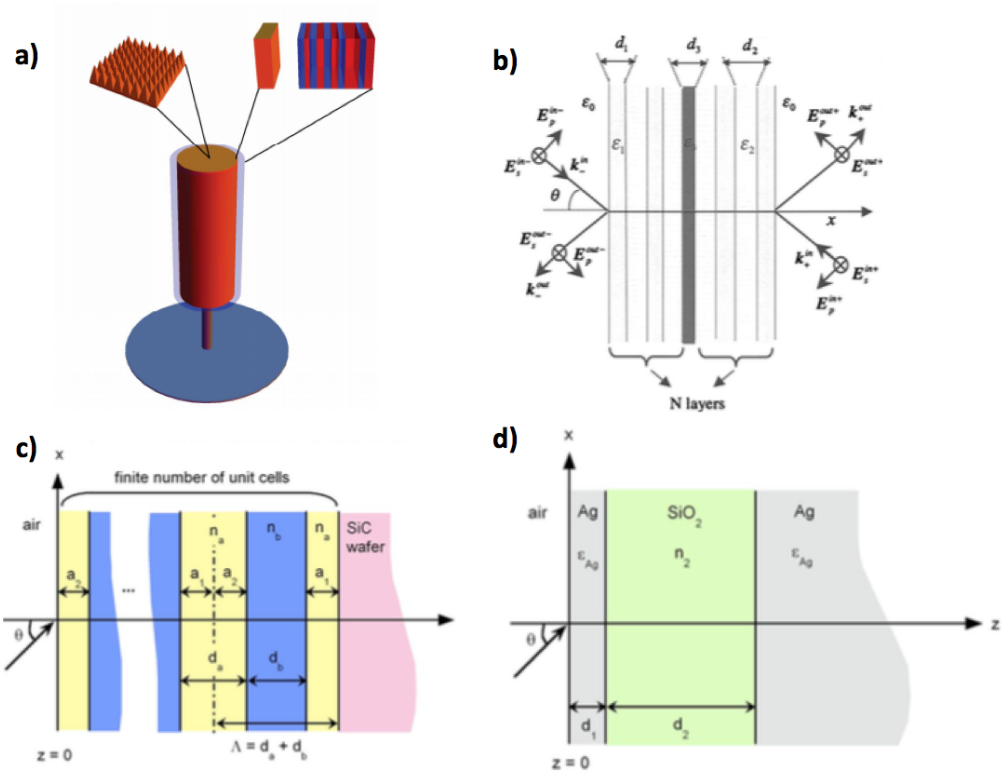

Fig. 5: Illustration of various planar structures amenable to design and modeling by transfer matrix methods that serve as selective emitter structures. A 1D photonic crystal integrated into a STPV absorber/emitter structure is is illustrated in **(a)**. Further details, including absorptivity spectra from this class of structures, can be found in Fig. 6 and in [60]. A Bragg reflector with a single absorbing defect layer, which supports spectrally selective emission modes, is illustrated in **(b)**. Further details, including emissivity spectra from this class of structures, can be found in [61]. A structure that achieves angular and spectral selectivity by coupling evanescent photonic crystal modes to surface phonon polariton modes in a polar layer is illustrated in **(c)**. A structure that achieves angular and spectral selectivity by coupling incident light into Fabry-Pérot resonances is illustrated in **(d)**. Further details, including emissivity spectra from these classes of structures, can be found in [62]. Figures reproduced from [60–62] with permission.

the Transfer Matrix Method has been successfully applied for designing multi-layer absorbing structures that find wide use in TPV/STPV applications [61–63]. The computational effort of the Transfer Matrix Method is minimal as it primarily involves the computation of the matrix elements $M_{i,j}$, which can be accomplished in a number of arithmetic operations that scales linearly with the number of layers in the structure. The Transfer Matrix Equations can also be used to compute the dispersion for resonant modes in multi-layer structures. Two resonant modes of particular interest for multi-layer structures with one or more absorbing layers include surface plasmon polariton (SPP) modes [55,66–69], and perfectly absorbing (PA) modes [69–72]. SPP modes occur when $R \to \infty$ and $T = 0$, while the latter occurs when $R \to 0$ and $T = 0$ [69]. SPPs involve collective electronic oscillations coupled to a propagating electromagnetic wave, and they allow light to be guided along the 2-dimensional interface between a metal and a dielectric

layer. Because SPP wavevectors lie beyond the light-line (i.e. they have wavevector magnitudes larger than that of light propagating in the dielectric layer), excitation of SPPs can occur only under certain conditions. A classic technique for exciting SPPs, known as the Kretschmann-Raether configuration [73], involves an asymmetric dielectric/metal/dielectric structure with the refractive index of the dielectric substrate being larger than the refractive index of the dielectric superstrate. While normally incident light cannot couple into SPPs on specular surfaces, it can couple into SPP modes at the metal/superstrate interface if it is incident from substrate side at an appropriate angle. Using the Transfer Matrix Method to find the wavevector components that lead to the SPP condition ($R \to \infty$ and $T = 0$) in such an asymmetric structure is equivalent to finding the angle that allows coupling of light into the SPP via Kretschmann-Raether excitation. [69, 73] Scattering at the surfaces, for example because of surface roughness or patterning with nanoparticles, can also produce large wavevector components that will allow light to couple into SPPs even at normal incidence. Perfectly absorbing modes can allow perfect absorption of incident light by thin absorbing layers. Unlike SPPs, PA modes are non-propagating and do not necessarily lie to the right of the light line; in these cases, light can couple into perfectly absorbing modes in symmetric structures. [69]

2.5. Design of selective emitters for thermophotovoltaic applications using Transfer Matrix Methods

The resonant properties of multi-layer planar structures can be exploited for designing highly-selective emitter structures for use in thermophotovoltaic (TPV) and STPV devices. In TPV devices, thermal energy is transferred to a spectrally-selective emitter structure. The radiation wavelength of the emitter should be well matched to a PV cell bandgap so that its thermal emission can be efficiently converted to electrical current. TPV systems can harvest thermal energy as waste heat from engines or other sources. An STPV system is simply a TPV system that harvests thermal energy from solar radiation, and involves a good solar absorber as one of its components. The design of both absorbers and emitter structures has been the focus of considerable theory and modeling effort. Figure 5 illustrates several optimized planar emitters that were designed using Transfer Matrix Methods [10, 61, 62].

Despite their simplicity, multi-layer planar structures can support a rich number of interesting and controllable optical phenomena which can be exploited for TPV and STPV applications. One-dimensional photonic crystals (1DPCs) can be used in conjunction with absorbing materials to enhance the spectral and/or angular selectivity of absorption and emission [60] in an integrated absorber/emitter STPV structure. The evanescent modes supported by 1DPCs can also enable coupling into resonant surface waves in near and mid-IR frequencies, including surface plasmon polariton and surface phonon polariton modes, respectively [62], which gives hybrid structures consisting of hybrid 1DPCs and either a metal (strong near IR absorber) or a polar material (strong mid IR absorber) exceptional angular and spectral selectivity. Similarly, Ben-Abdallah and Ni have shown that coupling between localized defect states and surface waves can give rise to strong spectrally coherent emission when a single absorbing defect layer is introduced into a Bragg stack [61].

Given the diversity of possible planar structures, a vast parameter space exists for their design, and optimization methodologies must be chosen judiciously. Drevillon and Ben-Abdallah [74], as well as Nafzaoui, Drevillon, and Joulain [75], have developed robust optimization methodologies that steer multilayer structures to an optimal emissivity profile. The optimum of the emissivity profile can be defined in a variety of ways with respect to variables including the PV cell and operating conditions. One such approach for defining such a profile involves using the spectral efficiency of the emitter as a figure-of-merit, where the spectral efficiency depends on the emissivity of the structure, the band-gap of the PV cell, and the

target temperature of operation (see section *4.2*). The emissivity can be computed from the reflectance and transmission using the Transfer Matrix Method, enabling efficient computation of the figure-of-merit. The design problem can then be formulated as a maximization of the figure-of-merit in terms of the geometry and material properties of the emitter structure. This approach has been employed to design 1D photonic crystals involving tungsten and dielectric layers with spectral efficiencies of about 53% [76] (see Table 2). Similarly, the Transfer Matrix Method can be used to design broad-band absorbers, and has led to the prediction of absorption efficiencies of 74% in 1D photonic crystals made of tungsten and dielectric layers [76] (see Table 1).

A different Transfer Matrix Method-based approach for the design of STPV components, recently introduced by us, leverages the observation that structures that support perfectly absorbing modes with certain characteristics can perform as exceptional selective emitters. These characteristics, described in detail in [63], can be encoded directly into a search routine that allows for the identification of structure geometries that support these modes. The optimization over the figure-of-merit is therefore replaced with a search for a zero in T and R, which is equivalent to finding a zero in the transfer matrix element $M_{2,1}$ under the condition that the transmission is also zero, which can be easily satisfied. This approach has predicted structures with spectral efficiencies of 68% at operating temperatures of 1750 K when coupled with common PV materials [63].

2.6. Finite-Difference Time-Domain method

For the optical behavior of more general structures, numerical approaches must be employed to solve Maxwell's equations. Perhaps the most conceptually simple approach is known as the finite-difference time-domain (FDTD) method. Here the time evolution of the fields is computed using Maxwell's equations (the curl equations) where the spatial and temporal variables are discretized on a rectangular grid, and centered finite-differences are used for the derivatives in terms of these variables [42]. The electric and magnetic fields are spatially staggered on the computational grid, which enforces Gauss' law. Quantities such as absorption, scattering, reflection, and transmission can be defined in terms of fluxes of electromagnetic fields. Electric field distributions and other quantities may be obtained in the frequency domain by the appropriate Fourier transform of the time-domain fields. The permittivity of metals and semiconductors can have strong frequency dependence across the UV/Vis/IR spectrum, and this frequency dependence requires some consideration for time-domain simulations like FDTD. Material dispersion leads to time-dependence of the material susceptibility and causes the polarization density to depend on field values at all previous times. This is commonly handled by fitting the permittivity to an analytical function of frequency, commonly a sum of Drude and Lorentz oscillator functions, so that the convolution can be easily computed. A practical drawback is that it can be difficult to obtain a good fit for these functions across a broad spectrum for highly-dispersive materials.

The computational effort of FDTD scales with the 4^{th} power of the computational domain for simulations with 3 spatial and 1 temporal dimension. The spatial grids are generally discretized with grid spacing d, where d is a value less than the sub-wavelength electromagnetic field variations of interest in the complex optical response media being studied. (In such media, suitable values of d such that the results are converged must be determined empirically.) The time-step is usually defined relative to the spatial grid size by the Courant factor [42]. This tends to make simulations of structures with several disparate length-scales challenging, as a small grid size is required for the smallest feature, while many grid elements are required to span the physical structure. However, FDTD implementations can utilize multi-resolution grids to reduce the computational effort in these cases. Furthermore, FDTD simulations can

exploit symmetry, periodicity, and can be massively parallelized, all of which has enabled their application to a variety of complex systems. Of particular relevance to modeling the emission from the nanostructures of interest are recent FDTD developments that allow direct FDTD modeling of emissivity and near-field radiative heat transfer [77–80].

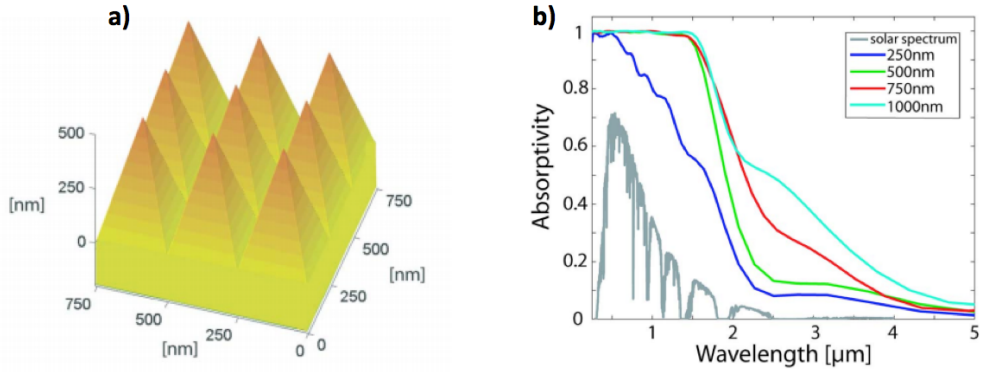

Fig. 6: Illustration of a tungsten structure whose absorptivity can be tuned by patterning of the surface. In this example, the tungsten structure is patterned with nanopyramids with various pyramid heights and with period fixed at 250 nm. A representative structure with a pyramid height of 500 nm is shown in **(a)**. Absorptivities of textured tungsten structures are plotted in **(b)** for a variety of pyramid heights with the period of the pyramids fixed at 250 nm. The finite-difference time-domain (FDTD) method was used to compute the absorptivities shown in **(b)**. Figures reproduced from [10] with permission.

2.7. Design of patterned structures for absorption enhancement using the FDTD method

Extensions of the previously-discussed multi-layer planar structures involve introducing geometric features in the lateral dimension(s). These types of structures include 2D and 3D photonic crystals, metasurfaces, metamaterials, and random-textured materials. FDTD can be a powerful tool for designing these types of structures, and can be particularly efficient when symmetry and/or periodicity can be exploited. Often, these sorts of patterned materials are desired to enhance the absorption of visible light, for example, to design a perfect absorber across the solar spectrum for solar thermophotovoltaic applications. For such an application, the transmission, reflection, and absorption can be computed across the spectrum as features of the surface are varied. This procedure is illustrated in Figure 6 (a) and (b), where the absorptivity of a tungsten surface patterned with pyramidal structures is computed by the FDTD method [60]. Similarly, Atwater and co-workers have employed FDTD simulation to design ultra-thin patterned surfaces that behave as broad-band "super absorbers" capable of enhancing conversion efficiency in thin-film PV materials [81]. Several of the current authors have utilized FDTD simulations to study and design tungsten absorber surfaces patterned with nanocones with absorption efficiencies of 80% [35] (see Table 1), as well as tungsten blazed grating emitter surfaces with spectral efficiencies of 59% [40] (see Table 2).

Many codes like Lumerical [82], a commercial-grade FDTD simulator, and MEEP [43], an open-source FDTD code, have scripting capabilities and other built-in tools to perform sweeps and optimizations over system variables, including material constants and geometric parameters. These sorts of scripting interfaces also allow the computation of more sophisticated quantities; for example, the net energy flux between isolated structures may be desired to optimize near-field radiative heat transfer [78].

2.8. Discrete Dipole Approximation

Several computational methodologies for solving Maxwell's equations in the frequency domain are also available, and here we focus on the Discrete Dipole Approximation (DDA), which is particularly useful for problems involving scattering and light absorption from particles. The idea behind DDA is to represent scattering structures by an array of N dipoles. It is important to note that in practice N is generally large, i.e. the particle or particles in the problem are being described by many dipoles filling their volumes and so that multipolar interactions can be correctly described. DDA is thus routinely used as a rigorous computational electrodynamics method and so its name is somewhat deceptive.

In DDA, each dipole has a polarization given by $\mathbf{P}_j = \alpha_j \mathbf{E}_j$, where $\mathbf{E}_j$ is the electric field at the discrete point occupied by dipole j, and α_j is the polarizability of dipole j, which is determined from the permittivity of the material being modeled [46]. The electric field at the position j of a given dipole is expanded as

$$\mathbf{E}_j = \mathbf{E}_{inc,j} - \sum_{k \neq j}^{N} \mathbf{A}_{j,k} \mathbf{P}_k. \tag{2}$$

The incident field ($\mathbf{E}_{inc,j}$) has the form of a monochromatic plane wave, and the product $-\mathbf{A}_{j,k}\,\mathbf{P}_k$ gives the electric field at point j due to the polarization at point k; hence, the matrix $\mathbf{A}$ carries information about the geometry and polarizability of the dipoles. The polarization is found by solving the system of linear equations given by $\sum_{k=1}^{N} \mathbf{A}_{j,k}\,\mathbf{P}_k = \mathbf{E}_{inc,j}$, where the diagonal elements of $\mathbf{A}$ have the known form $\mathbf{A}_{jj} = \alpha_j^{-1}$. Iterative methods are used to solve this equation, leading to overall quadratic scaling of the computational effort with the number of dipoles [46]. The optical cross sections may be written in terms of the polarization of the dipoles [46].

In general, high resolution can be obtained for small structures with a relatively small number of dipoles, and so DDA can be extremely efficient for modeling the optical properties of nanoparticles. DDAs formulation in the frequency domain also makes it more convenient than FDTD for modeling materials whose permittivity depends strongly on frequency since the permittivity as a function of frequency can be fed directly into the simulation. While scattering is solved for one frequency at a time, DDA can be run in parallel over the desired frequency range. One considerable drawback is that convergence of the DDA method, both in terms of the number of iterations for solving the linear equations and in terms of the accuracy of the polarization with respect to the number of dipoles, can be quite challenging for materials with large real or imaginary components of refractive index [83]. Silver is a classic material for which DDA modeling presents a particular challenge at visible frequencies.

Interesting recent developments in DDA of relevance to the problems of concern in this review include variations of DDA that are capable of describing particle-surface interactions [84] and near-field radiative heat transfer [85].

2.9. Design of nanostructures for near-field enhancement of solar energy conversion using the DDA method

Concentration of incident optical energy into the near-field of localized surface plasmons supported by nanostructures can also be leveraged to enhance solar conversion efficiency in PV materials. This approach is complementary to the one discussed with anisotropic scattering because it exploits the absorption of the nanostructure(s) rather than the scattering. The optical energy concentrated in the near-field of the plasmon can directly excite particle-hole pairs in a PV material with high efficiency if the absorption rate of the PV material is larger than the plasmon damping rate (equivalently, the inverse lifetime of the plasmon excitation) [55]. Therefore, nanoparticle systems with high near-field intensities and long plasmon lifetimes are ideal

for these applications. The large cross sections of plasmonic particles can also be leveraged to increase absorption efficiency in absorber structures in STPV applications. DDA methods can efficiently compute near-field distributions, absorption cross sections, etc, for multiple particles with complex geometries and sharp asperities that are separated by small-gaps, which are structures that typically give rise to exceptional near-field enhancement and large absorption cross sections. Plasmon lifetime information can be obtained from a Fourier transform over the absorption spectrum that is generated directly by DDA simulations run over a desired frequency range. Because the DDA method captures the fully coupled optical response of assemblies of nanostructures, it could be used to obtain an exact description of the absorption efficiency of the distribution of core-shell nanoparticles leveraged by Halas and co-workers for absorption enhancement [57] (see Figure 4).

2.10. Summary and outlook for theoretical design methodologies

We have described a number of powerful theoretical methodologies that can be put to use to understand, predict, and even tailor the optical response of systems of simple or complex nanostructures. The use of these methods, along with the ingenuity of many researchers, has allowed the design of many novel and useful systems for radiative control. However, as will be discussed in more detail in the remaining sections, overall conversion efficiencies of TPV/STPV systems often fall around 3-8%, well short of the theoretical limit of 85%. A significant challenge remains in integrating various theoretical methodologies to model and optimize global device performance [4, 9]. In principle, nanostructured systems may be designed or discovered by coupling the various electrodynamics modeling approaches described above to global optimization methods. Generally, an appropriate figure-of-merit to be maximized is identified, e.g. the spectral efficiency which will be discussed in detail later, and repeated calculations of the figure-of-merit are carried out while adjusting the features of the nanostructure until a global optimum is found. A plethora of multi-parameter optimization methods are available and have been used in the context of optimizing the optical response of nanostructures, including clustering algorithms [4], the Simplex method [57, 86], genetic algorithms [74, 87], particle swarms [75, 88], and Gaussian process modeling [89]. Certainly one challenge is that an integrated TPV/STPV system must couple together various optical modalities for absorption and emission. Usually, this requires abandoning exact analytical approaches in favor of approximate (e.g. perturbative) analytical approaches like coupled-mode theory. Alternatively, researchers must rely on the use of the numerical methodologies described above, though this may prove daunting from a computational point of view due to the multi-scale nature of these systems. Global system optimization must also include considerations like thermal management along with electrodynamics, as the requisite operating temperatures can lead to oxidation or deformation of the constituent structures and degradation of the device performance. Consideration of these various system parameters creates a highly heterogeneous optimization problem and presents significant challenges for global optimization. However, several authors including Celanovic and co-workers [4] as well as Wang and co-workers [9] have taken on the challenge of designing systems with optimal device consideration, which have led to device efficiencies approaching 3% and 10%, respectively.

3. Large area fabrication of optical nanostructures

3.1. Direct laser writing and laser interference lithography

A high power laser beam focused to sub-micron dimensions allows direct ablation of surface material, as shown in Figure 7(a), to form periodic or non-periodic structures. Alternatively, selective exposure of a photoresist can create feature sizes of about 0.5 microns [90].

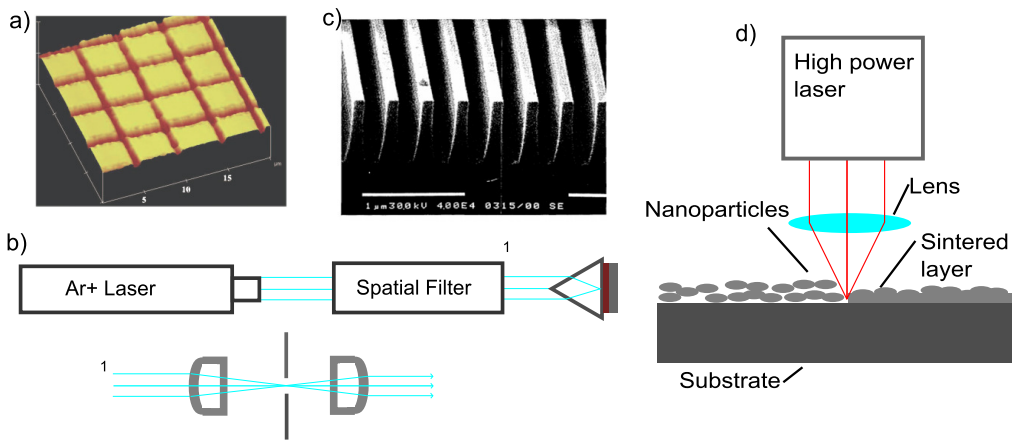

Fig. 7: a) AFM photograph of a micromachined double periodic structure with line-widths less than a micron [90] (reproduced with permission), b) Experimental setup for laser interference lithography, c) SEM image of gratings fabricated by laser interference lithography and etched into quartz [91] (reproduced with permission), and d) experimental setup for laser sintering of nanoparticles.

To obtain feature sizes of few hundred nanometers over a large area, laser interference lithography is ideal [91]. In interference lithography, a laser beam is split into two components, which can be recombined to form an interference pattern, as shown in Figure 7(b).

The period, P, of the grating is determined by $P = \frac{\lambda}{2n\sin(\theta)}$ where λ is the wavelength of the laser light, n is the refractive index of the medium and θ is the angle between two beams. For a wavelength of 442 nm, a surrounding medium index of 1.5, and an angle between the two beams of 60 degrees, line-widths of about 200 nm will be generated. Figure 7(c) shows a scanning electron microscope (SEM) image of the periodic pattern obtained with a He-Cd laser. This technique can allow the fabrication of large area patterns on various substrates. An exposed photoresist mask is used to etch the pattern on the substrate materials.

This method will be well suited for the fabrication of spectrally-selective surfaces as needed for STPV and TPV systems. The selective spectral emission wavelength and the efficiency of the emission can be controlled by the period, height and spacing between lines.

3.2. Laser sintering of nanoparticles

To achieve nanoscale roughness, nanoparticles dispersed in a liquid can be coated on a substrate [92]. A laser sintering process is then used to fuse the nanoparticles together by the high temperature generated by laser light absorption. In this process, the nanoparticles also get bonded to the substrate. The laser sintering process is shown in Figure 7(d). By controlling laser processing parameters such as optical power, scan speed, and beam overlap, different surface morphologies can be achieved. This fabrication method is well suited for solar thermal applications where high solar absorptance and low thermal emission is required.

3.3. Glancing angle deposition (GLAD)

Highly light-absorbing surfaces can be generated by micro-scale roughness due to the multiple reflections within such surfaces that effectively trap the incident light. Thin films of various materials, when deposited at large angles of incidence relative to the substrate and under vacuum conditions, give rise to cone like structures as shown in Figure 8(a) [93]. The deposited films

look black to the naked eye because of their extremely high optical absorption. The absorption efficiency of these structures can be controlled by the height of, and spacing between, the pillars. The glancing angle deposition method can be used to enhance solar light absorption and to fabricate spectrally-selective surfaces

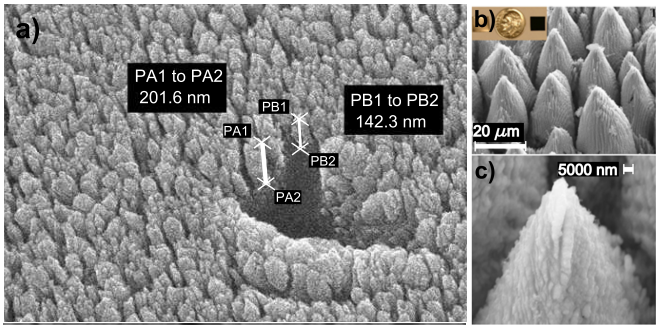

Fig. 8: a) SEM image of GLAD structures (reprinted with permission) [94] and b) and c) SEM images of a laser micro/nano textured Ti surface (reprinted with permission) [28].

3.4. Laser micro/nano textures

Micro- and nano-textured surfaces can be obtained when a high power laser beam is focused on a substrate and laser processing is carried out within a certain power and scan speed range [28]. The details of the texture, including height and spacing, can be controlled by laser processing parameters. The properties of the textured surface allow control over the absorption efficiency of the surface. Figure 8(b) and 8(c) show SEM images of a laser microtextured Ti surface.

Multi-layer thin films composed of metal dielectric layers can also be designed such that high optical absorption can be achieved. Reciprocally, the emissivity of multi-layer structures can be tuned over a narrow spectral range. Figure 2(c) shows an example of thin film structure to control the emission properties.

The high solar radiation absorption can be achieved by fabrication techniques such as metal-dielectric multi-layer structures, surface microtexturing and by the use semiconductor-metal layer structures. The spectral selective emittance can be achieved by fabrication of photonic crystal structures using standard optical or e-beam lithography method or by the use of periodic/non-periodic submicron surface textures. The microtexture fabrication method is suited to achieve black surfaces with extremely high ($>$95%) light absorption over broad wavelength and incident angle ranges.

4. Solar energy conversion applications

4.1. Solar thermal

Solar thermal (ST) systems are solar powered devices that generate energy via a heat engine. Incoming solar energy is concentrated on an absorbing surface, which is heated to high temperatures. A heat exchange fluid is then used to draw energy from the absorbing surface to the heat engine. Since heat engines can be more efficient at higher operating temperatures, ST systems operate at high temperatures, up to 1000°C.

Operating at such high temperatures means that there will be a large amount of thermal emission from the absorbing surface, resulting in a loss of energy. To reduce this loss, the thermal emittance of the absorbing surface must be minimized. Here, we will define ε_{abs} as the thermal emittance of an absorbing surface held at a specific temperature relative to the thermal

emittance of a blackbody held at the same temperature. This means that an absorbing surface with an ε_{abs} of 0.5 at 1000°C would have half the thermal emission of a blackbody at 1000°C. Note that the ε_{abs} of a surface can change drastically with temperature if its reflectivity and absorbance change for different wavelengths of light. This is because the spectral composition of blackbody radiation changes with temperature. At the same time, the solar absorptance (α_{sol}) of the surface must be maximized to ensure a high power input into the device.

For a surface to have high α_{sol} and low ε_{abs}, it must have a low reflectance and high absorbance in visible wavelengths (where most solar light is located), and a high reflectance in the near infra-red (NIR) region (where most thermal emission is located). This is a type of spectrally selective surface. These surfaces must also remain stable under the high operating temperatures found in ST systems. The relative importance of high α_{sol} and low ε_{abs} can change due to changes in system parameters. For example, higher operating temperatures increase thermal emission and place more importance on achieving a low ε_{abs}, while higher solar concentrations result in achieving a high α_{sol} being more important.

Spectrally-selective surfaces are much studied in ST research because they can lead to high-efficiency systems. While coatings for lower (<500°C) temperatures have been extensively studied, they are generally not suitable for high temperature operation due to a lack of thermal stability [95]. Some research has attempted to use silicon or germanium based absorbers, but their high solar reflectance necessitates the use of broad-band anti-reflective coatings which results in high ε_{abs}, and their performance degrades at high temperatures due to oxidation [96].

Stacks of layered dielectric and metallic films can be used to control the reflectance of structures via multiple reflections and interference effects [97]. Many different materials have been investigated for this purpose, including stacks using tungsten, molybdenum, titanium oxide, and magnesium fluoride that had an $\varepsilon_{abs}<7\%$ and $\alpha_{sol}>94\%$ [96,98,99]. Unfortunately, fabrication of these surfaces requires vacuum deposition of multiple layers with precise thickness, which can be difficult.

Ceramic-metal composites (cermets) consist of metallic particles in a dielectric host that are often used as spectrally selective surfaces in ST applications. The metallic particles in the cermet layer result in high α_{sol} due to multiple reflections, and they are typically used on metallic substrates with high IR reflectance, resulting in low ε_{abs} [96, 100–106]. The disadvantages of cermets include sensitivity to oxygen at high temperatures and the requirement for vacuum fabrication methods.

Nanotextured surfaces can be stable at high temperatures when they are formed from high melting point metals such as tungsten and tantalum and are coated with a protective oxide [34]. They also lend themselves to fabrication using the methods described in this report. Because these methods take advantage of surface geometry, they do not require multiple materials, resulting in a high thermal stability. Indeed, nanostructures of tungsten coated with a protective hafnium coating have been shown to be stable to temperatures of 1100 °C in air [34,107]. Tantalum photonic crystals have also been reported to be stable at temperatures of over 1000°C [108].

Periodic sub-wavelength gratings on tungsten substrates have been fabricated with an α_{sol} of 82% and ε_{abs} of 5.6% at 770°C and were experimentally verified to be stable up to temperatures of 900 °C [50]. These structures cause standing wave resonances that can be tuned for solar absorption.

Sub-wavelength roughness on metallic substrates can also increase solar absorbance due to the surface acting as a graded index medium [50,109]. The ε_{abs} of these surfaces can be kept low because NIR wavelengths are much longer than the dimensions of the roughness, so the surface appears smooth [110]. An advantage of these types of structures is that they do not require periodicity, and randomness can in fact be an advantage [35]. Simulations have shown pseudo-random nanocones on a tungsten substrate to have an α_{sol} of 97% and ε_{abs} of 16% at 1400

°C [35]. Experimental data on surface roughness created by laser-sintering of nanoparticles have shown an α_{sol} of 83% and ε_{abs} of 11.6% [23].

4.2. Solar thermophotovoltaics

Typical STPV systems consist of an absorbing/emitting structure that is held under vacuum to reduce convective losses and increase thermal stability [32, 111]. Then, sunlight is focused on the absorbing surface of the structure, where it is absorbed and converted into thermal energy. This results in the absorbing/emitting structure becoming very hot, with temperatures up to 1750 K common in these systems. As the system temperature rises, it begins to emit a large amount of thermal radiation. The portion of thermal energy that is emitted by the emitting surface can then be collected by a PV cell and converted into electrical energy. An additional advantage of STPV systems is their ability to store absorbed energy as heat, which is more efficient than battery storage with traditional PV cells. STPV technology can also be easily adapted to thermophotovoltaic (TPV) systems, which operate similarly but use a burning fuel or waste heat as a thermal source instead of the sun. By transforming the incoming solar radiation from a broad-band source to a more narrow-band one, STPV systems can operate at efficiencies exceeding the Shockley-Queisser limit of 44% for silicon PV cells operating under diffuse radiation [112]. In fact, the upper *theoretical* limit for STPV system efficiency is 85.4% [96].

Table 1: Efficiency, relative solar absorption, and relative thermal emission at a temperature of 1700 K of selected absorbing surfaces.

Absorber type	Absorber efficiency	α_{sol}	ε_{abs}
Ideal solar absorber	0.83	0.87	0.04
Pseudo random nano-cones in W	0.80	0.97	0.16 [35]
W pyramidal nanostructures	0.79	0.92	0.13 [60]
Mo-SiO_2 cermet	0.77	0.93	0.16 [113]
Carbon nanotubes	0.74	0.99	0.95 [114]
1-D photonic crystal on W	0.74	0.80	0.06 [76]
Blackbody absorber	0.73	1.00	1.00
Anti-reflection coating on W	0.67	0.73	0.05 [76]
W cavities	0.59	0.74	0.15 [115]
Surface-relief grating on W	0.49	0.53	0.05 [36]
Bare W	0.41	0.44	0.04 [116]

The absorbing surfaces for STPV devices are similar to those used in ST systems, although higher operating temperatures (up to around 1750 K) make thermal stability a more prominent concern, and high levels of solar concentration (>4000) make a high α_{sol} of paramount concern. This means that nanotextured absorbing surfaces are a very good match for these systems. Most experimental STPV systems to date have utilized blackbody absorbing surfaces [114, 115, 117, 118], leaving room for much improvement by using selective absorbing surfaces. Recent results have reported record efficiencies [13, 76] using both selective absorbers and selective emitters. A yttria-stabilized zirconia and tungsten stack was used as a selective absorber in an experimental system [76], but while it's thermal emission was low, its performance was hindered by a low α_{sol} of 80%. Simulations of various surfaces have shown large gains in system efficiency from the use of nanotextured selective, such as pseudo-random nanocones with an α_{sol} of 97% and ε_{abs} of 16% [35], or pyramidal nanostructures in tungsten with an α_{sol} of 92% and ε_{abs} of 13% [60] but none have been experimentally demonstrated in a working

STPV system to date [34, 36].

Various methods of evaluating STPV system performance exist, but in this work we will focus on the relative efficiencies of the individual surfaces of an STPV device. This allows us to directly compare different methods of making selective absorbing and emitting surfaces. Many parameters in STPV systems can effect the performance of these surfaces, so an operating temperature of 1450°C, a solar concentration of 2500, and a GaSb solar cell are assumed here due to their prevalence in STPV systems [10,35,40,115,117,118]. This provides for a good relative comparison of different surfaces, although it is not a measure of overall device efficiency.

Table **??** shows the α_{sol} and ε_{abs} of some absorbing surfaces, as well as a calculated surface efficiency. The quantity η_{abs} is given by

$$\eta_{abs}(T) = \frac{\int_0^\infty \{E_{inc}(\lambda)\alpha(\lambda) - \varepsilon(\lambda)B(\lambda,T)\}\, d\lambda}{\int_0^\infty E_{inc}(\lambda) d\lambda} \tag{3}$$

$$E_{inc}(\lambda) = C\, \eta_{conc}\, E_{sun}(\lambda), \tag{4}$$

where $\alpha(\lambda)$ is the spectral absorption of the surface, $\varepsilon(\lambda)$ is the spectral emittance of the surface, C is the concentration ratio of incoming sunlight, η_{conc} is the solar concentration efficiency, $E_{sun}(\lambda)$ is the spectral irradiance of the sun at the earth's surface, $B(\lambda,T)$ is Planck's law for blackbody radiation, and $E_{inc}(\lambda)$ is the spectral energy incident on the absorbing surface.

For emitting surfaces, a similar approach to absorbing surfaces can be taken, but with a focus on low reflectance in a narrow peak near a specific wavelength (which depends on the bandgap energy of the PV cell used), as opposed to a broad low reflectance band in the visible region. To accurately compare emitting surfaces, their spectral efficiency is used.

The spectral efficiency is given by [40]:

$$SE = \frac{\int_0^{\lambda_{bg}} \frac{E_{bg}}{E_\lambda} B(\lambda,T)\, \varepsilon_S(\lambda)\, d\lambda}{\int_0^\infty B(\lambda,T)\, \varepsilon_S(\lambda)\, d\lambda} \tag{5}$$

where E_{bg} is the bandgap energy of the PV cell, E_λ is the energy of a photon with wavelength λ, and $\varepsilon_S(\lambda)$ is the spectral emissivity of the emitting surface, approximated as the surface's absorptivity. This gives the relative efficiency of the emitting surface, but does not represent an overall system efficiency.

Two structures work particularly well for this purpose: dielectric-metal stacks and 2-D or 3-D photonic crystals. A yttria-stabilized zirconia (YSZ) and tungsten stack was able to achieve highly selective emission and experimentally demonstrated to be stable at temperatures up to 1350 °C [76].

Many nanotextured emitting structures have been simulated to be extremely efficient [37]. These include blazed gratings on tungsten [40], complex square gratings on tungsten [38], micro-cavities in tungsten [33], tungsten surface gratings [36], 3-D photonic crystals [120], and metamaterials [121]. Table **??** shows the spectral efficiencies of some of these surfaces. This shows a large increase in efficiency for selective emitters over blackbody emitters. While experimental systems using these structures have not yet been realized, they promise large efficiency gains for the future. Table **??** shows the electrical efficiencies of some simulated and experimental STPV systems. The simulations outlined here show a large difference in predicted efficiency; however, a significant portion of this variation is caused by simulation parameters. Since there is no standard for simulated STPV systems, some papers use an ideal model where only losses due to the surfaces are accounted for, while others use a more realistic model that encompasses many losses. Namely, references [10] and [32] assume ideal PV cells, ideal solar concentrators, and assume an ideal view-factor between the emitting surface and solar cells.

Table 2: Optical efficiency of selected emitting surfaces at 1700 K [119].

Emitter type	η_{emit}
Ideal emitting surface	0.84
Periodic hole array on W	0.64 (simulated)
Blazed grating on W	0.59 [40]
Anti-reflection coating on W	0.59 (simulated)
Complex square grating on W	0.53 [38]
1-D photonic crystal on W	0.53 [76]
Micro-cavity in W	0.51 [33]
$Al_2O_3/Er_3Al_5O_{12}$ eutectic composite	0.41 [117]
Blackbody emitter	0.29

References [33], [119], and [14] attempt to model PV cell losses and realistic absorbing and emitting surfaces. Some of the remaining difference between efficiencies in the modeled systems is also due to differences in assumptions between simulations.

Despite the assumptions in these models, they clearly show that nanostructured surfaces are extremely important to ensure adequate spectral selectivity in these systems. While reference [10] and [32] used many idealities, they clearly show that STPV systems are capable of having efficiencies above the Shockley-Queisser limit for single junction PV cells. References [33], [119], and [14] predict high potential operating efficiencies using realistic operating conditions. The primary reason that experimental systems lag behind simulations is because a lack of high quality nanostructures in these systems [76, 122]. The YSZ and W stack used in [76] proved to be a less efficient solution for both the absorbing and emitting surfaces than other surfaces examined in this article. In [122], secondary, less efficient surfaces had to be used for both the absorbing and emitting structures due to fabrication problems. Reference [76] uses a blackbody absorbing surface and is restricted to a low operating temperature which reduces efficiency. This points to a large increase in efficiency that can be achieved by using nanostructures to close the gap between experimental and theoretical devices. The simulation and fabrication methods outlined in this paper show that this is possible.

Thermophotovoltaic (TPV) systems are another important area for harvesting waste heat energy. The reported efficiency of TPV systems is low at around few percent. However, as demonstrated by Bermel et al. [4] by using spectral selective surfaces the calculated efficiency can be very high (26.2%). The calculation was based on operating temperature of 1200°C. Similarly, Foley et al. [63] has shown in the paper as part of this special issue that by using metal (Ag)-dielectric (Si_3N_4) structure the calculated efficiency of 10% can be achieved at low operating temperature of 1000°C. It can also be further enhanced by using selective filters and operating at 1200°C.

5. Conclusions

We discussed a variety of modeling and fabrication techniques for controlling light absorption and emission by nanostructures. Such control is important for solar and thermal energy conversion devices including traditional photovoltaic (PV), solar thermal (ST), and solar thermophotovoltaic (STPV) devices. The use of thermal energy conversion in particular, can circumvent some efficiency limitations on standard PV cells. We anticipate that significant efficiency improvements can be achieved in this area by building on the techniques discussed here. For example, while ST systems are already achieving high efficiencies in commercial use,

Table 3: Efficiency of selected STPV systems.

Absorbing surface	Emitting surface	PV cell	Temp. (K)	Efficiency (%)
Experimental systems				
Laser-textured W with Si_3N_4 coating	W with Si_3N_4 coating	GaSb	1777	6.2 [122] (2015)
YSZ and W stack	YSZ and W stack	GaSb	1640	8 [76] (2015)
Carbon nanotubes	Si/SiO_2 stack	InGaAsSb	1285	3.2 [114] (2014)
Graphite	W with HfO_2 coating	Ge	$\sim$1700	0.8 [118] (2012)
Tungsten cavity	Thin W film	GaSb	$\sim$2000	1 [115] (2007)
Graphite	$Al_2O_3/Er_3Al_5O_{12}$ composite	GaSb	Unmeasured	0.02 [117] (2000)
Simulated systems				
Pyramidal W nanostructures	Si/SiO_2 stack	GaSb	6000	49 [10]
Blackbody absorber	Monochromatic emitter	Ideal cell	2872	45.3 [32]
Selective absorber	W surface grating with Si/SiO_2 filter	GaSb	1920	23.4 [33]
Periodic hole array on W	Pseudo-random cones on W	GaSb	1700	14.4 [119]
2D Ta photonic crystal	2D Ta photonic crystal	InGaAsSb	1400	10 [14]

experimental TPV and STPV efficiencies remain low. The primary cause of lowered device efficiency is lack of control over the spectral emissivity of the absorbing and emitting surfaces. The nanostructures, simulation, and fabrication methods highlighted here can be used to greatly increase efficiencies in all three of these systems. Indeed, simulations of nanostructured devices show that extremely high efficiencies exceeding the Shockley-Queisser limit are achievable in TPV/STPV systems. For example, one of the most promising simulated devices have shown conversion efficiencies of 26.2% at system temperatures of 1200°C and a maximum conversion efficiency of 49% was predicted for system temperatures of about 2130 K [10]. However, the highest conversion efficiency measured for an STPV device is about 8% for 1D photonic crystal structures of composed of tungsten and YSZ at device temperatures of 1640 K [76]. This large gap in system efficiency is due to the lack of temperature-stable nanostructures and high losses in experimental STPV systems. Future theoretical design methodologies should involve explicit considerations of aspects like thermal properties of materials and the thermal deformation of nanostructures to guide the fabrication of structures that are more robust to thermal degradation. Additionally, management strategies including the use of ST systems in tandem with STPV systems to capture waste heat from the STPV device should be explored.

Acknowledgments

We would like to thank the NASA Langley Professor and NSF IUCRC programs for their support of this project. Part of this work was performed at the Center for Nanoscale Materials, a U.S. Department of Energy, Office of Science, Office of Basic Energy Sciences User Facility under Contract No. DE-AC02-06CH11357.